



SpeckleCam: high-resolution computational speckle contrast tomography for deep blood flow imaging

AKASH KUMAR MAITY,* MANOJ KUMAR SHARMA, ASHOK VEERARAGHAVAN,  AND ASHUTOSH SABHARWAL

Department of Electrical and Computer Engineering, Rice University, Houston, TX, USA

**akashmaity@ymail.com*

Abstract: Laser speckle contrast imaging is widely used in clinical studies to monitor blood flow distribution. Speckle contrast tomography, similar to diffuse optical tomography, extends speckle contrast imaging to provide deep tissue blood flow information. However, the current speckle contrast tomography techniques suffer from poor spatial resolution and involve both computation and memory intensive reconstruction algorithms. In this work, we present SpeckleCam, a camera-based system to reconstruct high resolution 3D blood flow distribution deep inside the skin. Our approach replaces the traditional forward model using diffuse approximations with Monte-Carlo simulations-based convolutional forward model, which enables us to develop an improved deep tissue blood flow reconstruction algorithm. We show that our proposed approach can recover complex structures up to 6 mm deep inside a tissue-like scattering medium in the reflection geometry. We also conduct human experiments to demonstrate that our approach can detect reduced flow in major blood vessels during vascular occlusion.

© 2023 Optica Publishing Group under the terms of the [Optica Open Access Publishing Agreement](#)

1. Introduction

Continuous blood flow is essential to the normal functioning of tissue and organs. Arteries and veins carry oxygenated and deoxygenated blood and lie deep within the human tissue (>1 mm from the skin surface). The nutrients and oxygen in the tissue are generally exchanged through smaller vessels that constitute the micro-vascular bed and are located closer to the skin's surface. Insufficient blood supply due to blockage of blood vessels might result in potential clinical complications. Microvascular blood flow or perfusion is an indicator of one's circulatory health, revealing any narrowing or blockage of blood vessels. Directly measuring vascular flow is challenging since the vessels are located deep within the tissue. Computed angiography and magnetic resonance angiography are non-invasive techniques for imaging blood vessels and have been used to diagnose vascular diseases, for example, peripheral arterial disease [1–3]. However, both these techniques are expensive and may require injecting contrast agents in the blood stream [1,4]. Optical techniques are therefore being explored as low-cost alternatives for obtaining deep tissue blood flow.

Laser Doppler Flowmetry (LDF) is a commonly used technique for obtaining a point estimate of microvascular blood flow [5,6] and has been extended to imaging applications (Laser Doppler Imaging) [7]. LDF uses a coherent source of light of a particular frequency to illuminate a region of the human tissue. When the incident light interacts with the moving scattering particles, mainly the red blood cells, it undergoes a slight change in frequency, also known as the Doppler shift. On the other hand, the light interacting with the static components, such as the tissue cells, is unaffected and retains the same frequency as the source. As a result, the Doppler-shifted light and the unaffected light interfere to produce random fluctuations at the detector. The power spectral density of the intensity fluctuation at the detector directly depends on the speed of the red blood cells. LDF is mostly used to recover microvascular blood flow [6]. Diffuse Correlation

Spectroscopy (DCS) uses point light sources and detectors separated by a distance to obtain blood flow information from deeper inside the tissue [8,9]. The main limitation of DCS is that it operates in a low signal-to-noise ratio regime [10], and needs detectors with high sampling speed (in order of MHz) to capture the intensity fluctuations, thereby limiting the number of detectors for obtaining spatial information.

Camera-based methods for imaging blood flow are being widely explored due to the advantage of providing spatial information in high resolution. The amplitude of subtle blood volume pulsations captured by camera pixels on the skin surface illuminated by an incoherent light is used as a surrogate measure of blood flow [11–13]. Laser speckle imaging (LSI) uses a coherent light source broadly illuminating the tissue surface and a CCD or CMOS camera to obtain superficial blood flow information with high spatial resolution. Speckle contrast tomography (SCOT) extends LSI to obtain blood flow information in three dimensions by using scanning point sources instead of broad illumination. Each camera pixel acts as a detector at various distances from the point sources, thereby capturing light that has probed different depths within the tissue. Laser speckle contrast tomography has been used to assess deep blood flow in the brain [14] and burn wound monitoring [15]. However, the current state-of-the-art techniques for recovering 3D blood flow have two limitations- i) memory and computation intensive algorithms which limits the spatial resolution of the reconstructed blood flow in 3D volume, and ii) poor depth reconstruction due to several approximations in the forward model.

In this work, we tackle the limitations of previous approaches by using a line-scanning system that allows us to i) develop an efficient forward and inverse model, resulting in a higher spatial resolution, and ii) use Monte-Carlo-based simulations for the forward model which results in better reconstruction of flow features at different depths in the 3D volume. Overall, our main contributions are as follows:

1. We use a line-scanning system consisting of a laser as an illumination source synchronized with a camera to obtain a dense set of speckle contrast measurements for various source-detector pair distances. We then develop a convolution-based inverse algorithm, shown in Fig. 1, to efficiently reconstruct the blood flow inside the volume with high spatial resolution; we can resolve 2 mm structures at a depth of 6 mm inside a tissue-like scattering medium.
2. We derive an efficient technique, SpeckleCam, to compute a perturbation-based sensitivity matrix using Monte Carlo simulations via the photon-replay method. We show that SpeckleCam improves the 3D reconstruction quality of structures along various depths inside the scattering medium using Monte Carlo-based sensitivity matrix over the traditional diffusion-based model.
3. We validate our approach on tissue phantoms containing hollow complex tube structures with controllable fluid velocity through the tubes. Our system is capable of resolving structures with a flow speed greater than 5 mm/s. We also image the human arm and wrist during varying blood perfusion stages induced by manual occlusion. We confirmed, as expected, a reduction in blood flow in major blood vessels lying >1 mm below the skin surface during different stages of blood occlusion.

The rest of the paper is organized as follows. First, we discuss the relevant background and prior work in Section 2. Next, we derive a model to describe speckle contrast images using diffusion approximation and perturbation-based Monte Carlo simulation in Section 3. We then introduce our convolution-based forward model and reconstruction algorithm in Section 4. Section 5 describes our hardware setup and the experiments to validate our approach. We discuss the reconstruction results using our approach in Section 6. Finally, we conclude with future scope and limitations in Section 7.

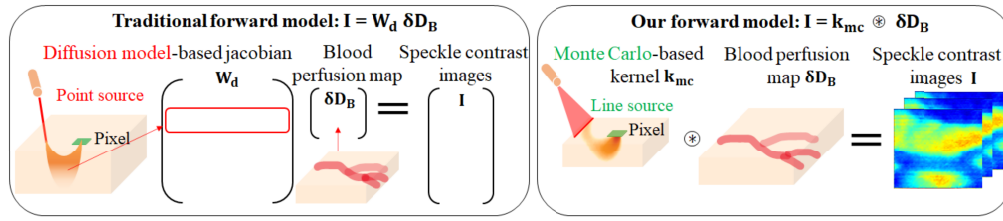


Fig. 1. Our proposed approach for high-resolution deep blood perfusion imaging. We replace the point light source with a line source and develop a convolutional forward model based on Monte Carlo simulations. The convolution-based forward model allows us to develop an efficient inverse algorithm in place of the traditional matrix inversion-based reconstruction process.

2. Background and key challenges

2.1. Speckle contrast imaging

Speckle contrast imaging system typically uses a red or infrared laser to illuminate a region on the surface of a scattering medium, mainly the tissue. Light gets scattered and travels different paths in the medium. Photons with resulting path length differences interfere constructively or destructively to produce random bright or dark spots on the detector. A camera captures a 2D image of this interference pattern, also known as the speckle image. In the case of dynamic scattering particles, for example, moving red blood cells, the speckle image changes temporally, and the fluctuation in the speckle image is directly related to the speed of the dynamic particles. A camera with a fixed exposure time records a blurry speckle image. The amount of blurriness depends on the speed of the scattering particles and is quantified by measuring contrast in a speckle image. The speckle contrast K of an image I is calculated as $K = \sigma(I)/\langle I \rangle$ where σ is the local standard deviation, and $\langle \rangle$ is the local mean of the speckle image. The local speckle contrast is measured spatially in a small $N \times N$ pixel neighborhood or in the temporal domain where consecutive frames are considered to calculate speckle contrast at a single pixel location [16–18]. In areas of increased blood flow, the speckle pattern blurring is more prominent, resulting in decreased contrast in the corresponding high blood flow areas.

Speckle contrast imaging uses a wide-field illumination; therefore, the detectors are most sensitive to the superficially scattered photons [19]. Furthermore, in reflection geometry, the signal contrast due to deep flow decreases with the thickness of the static scattering medium [20,21]. Speckle contrast imaging, therefore, has been mostly limited to superficial blood flow imaging. In an attempt to increase the imaging depth, the line-scan imaging technique is generally adopted [22–24] to reject surface reflections and improve sensitivity to blood flow in deeper tissue. However, as light penetrates deeper, it gets scattered numerous times inside the tissue. The result is a loss in spatial resolution at the expense of improved sensitivity towards deeper flow.

2.2. Speckle contrast tomography

Speckle contrast tomography extends speckle imaging toward recovering deep blood flow information. The idea is similar to Diffuse Optical Tomography (DOT), where point sources are used instead of wide-band illumination. The camera pixels at various distance from the light source records the backscattered light that has probed different regions inside the tissue volume. Under certain assumptions, a forward model relates the unknown blood flow at each voxel to the set of measurements by a linear set of equations. The flow at each voxel in a region is then reconstructed by fitting a forward model to the set of measurements [14,25,26]. The Correlation

radiative transport equation (CTE) is generally used to derive the forward model for speckle contrast tomography. However, the CTE does not have a closed-form solution and is typically solved either by mesh-based Monte Carlo simulation or by making diffuse approximations. Monte Carlo simulation offers very accurate solutions to CTE but is time-consuming. Given a dense set of measurements where each camera pixel acts as a detector, modeling the correlation function at thousands of detectors through traditional Monte Carlo simulations is practically infeasible. A faster approach is to use a diffusion equation to provide a lower-order expansion of the CTE and obtain a closed-form solution. However, the diffuse approximations often lead to loss of information, especially in the transport regime [27]. The Monte Carlo simulation or the analytical model is used to construct the sensitivity based on apriori known optical properties of a homogeneous medium. The heterogeneity modeled by a change in blood flow per voxel in a volume is generally reconstructed by inverting the sensitivity matrix. The number of voxels for reconstruction determines the size of the sensitivity matrix. Reconstructing for many voxels is not feasible due to the matrix-inversion step and therefore limits the spatial resolution of the reconstructed volume [25]. In [28], the authors tackle the poor resolution issue by using a high-resolution structural prior volume obtained via two-photon microscopy. A perturbation Monte Carlo model is then used to recover blood flow in high resolution. However, obtaining structural prior may not always be feasible.

3. Theory

In this section, we derive a forward model for laser speckle contrast images. We use this model to develop our reconstruction algorithm for obtaining high-resolution blood flow maps. Laser speckle contrast imaging mainly relies on the principle that when a coherent source of light is used to illuminate a specific point on the surface of a scattering sample, the constant movement of scattering particles causes fluctuations in the speckle images captured by a camera, as shown in Fig. 2. The constant fluctuations induce blurriness in the time-integrated speckle measurements, and the blurriness, quantified with speckle contrast, is directly related to the speed of the dynamic particles. The speckle contrast K is related to the electric field autocorrelation function as follows [29],

$$K^2 = \frac{2\beta}{T} \int_0^T g_1^2(\tau) \left(1 - \frac{\tau}{T}\right) d\tau, \quad (1)$$

where $g_1(\tau)$ is the normalized electric field autocorrelation function, T is the exposure duration of the camera, and β is a constant that depends on experimental conditions. Generally, in a densely scattering medium, the field autocorrelation function is defined as

$$g_1(\tau) = \int_0^\infty P(s) \exp[-k_0^2 \langle \Delta r^2(\tau) \rangle s / l^*] ds, \quad (2)$$

where s denotes the pathlength, $P(s)$ denotes the normalized distribution of pathlength s of photons in the scattering medium, l^* denotes the random photon walk length that depends on the scattering property of the medium, k_0 is the wavenumber that depends on the wavelength of light and $\langle \Delta r^2(\tau) \rangle$ models the RMS displacement of the moving scattering particles. For, Brownian motion, $\langle \Delta r^2(\tau) \rangle = 6D_B\tau$, where D_B is the particle diffusion coefficient, or $\langle \Delta r^2(\tau) \rangle = V^2\tau^2$ in case of a directed capillary flow, where V is the average fluid velocity. A way of generating the normalized autocorrelation function is first to generate the term $P(s)$, which depends on the scattering medium properties and is often difficult to obtain an analytical solution.

3.1. Analytical model based on diffusion approximation

A common approach to modeling the normalized autocorrelation function is to use the Correlation Transport Equation (CTE). The CTE is similar to the Radiative Transport Equation (RTE), which

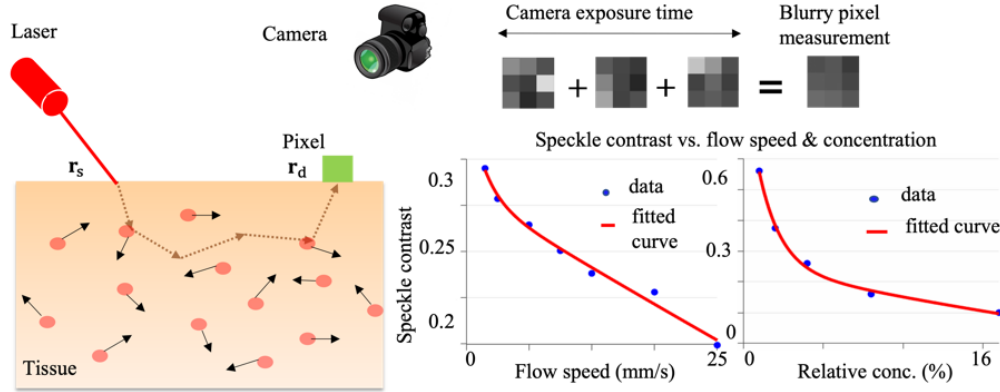


Fig. 2. A speckle contrast tomography setup in reflection geometry. A laser hits the surface of the scattering medium at location \mathbf{r}_s , and a camera captures the speckle image. The pixel measurement at location \mathbf{r}_d with a fixed camera exposure time captures a blurry speckle pattern due to light interaction with moving scattering particles. The local contrast in an image characterizes the blurriness. For a fixed camera exposure time duration, the speckle contrast decreases with the increasing flow speed and increasing concentration of dynamic particles.

models the photon flux in a scattering medium, the only difference being that the CTE models the autocorrelation function decay instead. Under diffusion and P1 approximation, the CTE is simplified to obtain an expression for the electric field autocorrelation function $G_1(\mathbf{r}, \tau)$ [30],

$$\left(-D(\mathbf{r})\nabla^2 + \mu_a(\mathbf{r}) + \frac{1}{3}\mu'_s(\mathbf{r})k_0^2\langle\Delta r^2(\tau)\rangle \right) G_1(\mathbf{r}, \tau) = S(\mathbf{r}), \quad (3)$$

where S is the light source, $\mu_a(\mathbf{r})$, $\mu'_s(\mathbf{r})$ are the absorption and reduced scattering coefficients respectively, and $D(\mathbf{r}) = 1/(3(\mu'_s(\mathbf{r}) + \mu_a(\mathbf{r})))$ is known as the diffusion coefficient of the scattering medium. The human tissue, modeled as a homogeneous scattering medium, consists of static cell particles and a capillary network that carries blood. The red blood cells flowing in the capillaries contribute to the decay in the field autocorrelation function, and the RMS displacement of the blood cells is given by $\langle\Delta r^2(\tau)\rangle$ and directly models the blood flow in human tissue. The tissue is commonly modeled as a homogeneous scattering medium with uniform optical properties (μ_a and μ'_s are independent of position \mathbf{r}), and the light source is placed at a location \mathbf{r}_s at the boundary of the medium. Under the conditions of semi-infinite geometry with extrapolated boundary conditions, the solution of the CTE is given by Green's function as [31],

$$G_1(\mathbf{r}_d, \mathbf{r}_s, \tau) = \frac{S}{4\pi D} \left[\frac{e^{-\alpha(\tau)r_1}}{r_1} - \frac{e^{-\alpha(\tau)r_2}}{r_2} \right], \quad (4)$$

where $G_1(\mathbf{r}_d, \mathbf{r}_s)$ is the normalized electric field fluctuation for a detector kept at a location \mathbf{r}_d . The term $\alpha(\tau) = \sqrt{\mu_a + \frac{1}{3}\mu'_s k_0^2\langle\Delta r^2(\tau)\rangle}$ governs how fast the field correlation function decays with τ . The term $r_1 = |\mathbf{r}_s - \mathbf{r}_d + z_0|$ and $r_2 = |\mathbf{r}_s - \mathbf{r}_d - z_0 - 2z_b|$ denotes the distance from the detector at \mathbf{r}_d to an isotropic source at $\mathbf{r}_s + z_0$ and its negative image source located at $\mathbf{r}_s - z_0 - 2z_b$, where $z_0 = 3D$, $z_b = (1 + R_{eff})D/(1 - R_{eff})$. The term R_{eff} models for the refractive index mismatch between the air and the scattering medium. The normalized correlation function is given by $g_1(\mathbf{r}_d, \mathbf{r}_s, \tau) = G_1(\mathbf{r}_d, \mathbf{r}_s, \tau)/G_1(\mathbf{r}_d, \mathbf{r}_s, 0)$. The speckle contrast $K_0(\mathbf{r}_d)$ at the pixel location \mathbf{r}_d is then given by Eq. (1).

In tomographic reconstruction problems, we are interested in locating spatial changes in blood flow inside the tissue. Tumors or blood vessels result in locally increased blood flow from the surrounding region. Assuming that the scattering and the absorption parameters remain constant, the perturbed particle displacement $\langle \Delta r^2(\tau) \rangle = \langle \Delta r^2(\tau)^0 \rangle + \langle \Delta r^2(\tau)^\delta \rangle$ reduces the speckle contrast due to the $\langle \Delta r^2(\tau)^\delta \rangle = 6\delta D_B \tau + \delta V^2 \tau^2$ term, which models the increase in blood flow. The reduced speckle contrast at the location \mathbf{r}_d for a given light source at \mathbf{r}_s is now given as,

$$K^2(\mathbf{r}_d, \mathbf{r}_s) = K_0^2(\mathbf{r}_d, \mathbf{r}_s) + \Delta K^2(\mathbf{r}_d, \mathbf{r}_s). \quad (5)$$

If we ignore the contribution from Brownian motion, we can write $\langle \Delta r^2(\tau)^\delta \rangle = \delta V^2 \tau^2$. The change in speckle contrast is derived from the modified normalized autocorrelation function in [25] and is then given by,

$$\Delta K^2(\mathbf{r}_d, \mathbf{r}_s) = -\frac{4\mu'_s k_0^2 \beta}{3T} \int W(\mathbf{r}_d, \mathbf{r}_s, \mathbf{r}_j) \delta V^2(\mathbf{r}_j) d\mathbf{r}_j, \quad (6)$$

where,

$$W(\mathbf{r}_d, \mathbf{r}_s, \mathbf{r}_j) = \int_0^T \frac{G_1(\mathbf{r}_s, \mathbf{r}_d, \tau)}{G_1(\mathbf{r}_s, \mathbf{r}_d, 0)} \frac{G_1(\mathbf{r}_s, \mathbf{r}_j) G_0(\mathbf{r}_j, \mathbf{r}_d, 0)}{G(\mathbf{r}_s, \mathbf{r}_d, 0)} \tau^2 \left(1 - \frac{\tau}{T}\right) d\tau, \quad (7)$$

where G_0 is Green's function and is related to Eq. (4) by $G_0 = DG_1/S$. The term W relates the change in blood flow inside the scattering medium to the change in speckle contrast recorded by the camera. The continuous scattering medium can be discretized into a set of voxels, and the medium properties are then defined for each voxel. The integral in Eq. (5) can then be replaced with a matrix multiplication operation, given as,

$$\Delta K^2(\mathbf{r}_d, \mathbf{r}_s) = -\frac{4\mu'_s k_0^2 \beta}{3T} \sum_{\mathbf{r}_j} W(\mathbf{r}_d, \mathbf{r}_s, \mathbf{r}_j) \delta V^2(\mathbf{r}_j), \quad (8)$$

where $W(\mathbf{r}_d, \mathbf{r}_s, \mathbf{r}_j)$ is called the sensitivity matrix and depends on the properties of the homogeneous scattering medium.

3.2. Perturbation model based on Monte Carlo simulations

The forward model derived in the previous section is based on lower-order approximations, which may not be very accurate. Monte Carlo simulation models light propagation within the tissue and are generally more accurate than analytical solutions. Therefore, we resort to Monte Carlo simulations to derive a direct solution to Eq. (1). With the same setup as in Fig. 1, we use MCX [32] to track photon scattering inside the medium. Specifically, the detector records the detected photon information, like the total momentum transfer and the total path length inside the medium. For a light source at location \mathbf{r}_s and a detector at \mathbf{r}_d , the normalized field autocorrelation function is given as,

$$g_1(\mathbf{r}_d, \mathbf{r}_s, \tau) = \frac{1}{N} \sum_{i=1}^N w_i \exp \left[-\frac{1}{3} Y_i k_0^2 \langle \Delta r^2(\tau) \rangle \right], \quad (9)$$

where for each photon packet i , $w_i = \exp[-\mu_a L_i] / \sum_{i=1}^N \exp[-\mu_a L_i]$, L_i is the total pathlength, and Y_i is the dimensionless total momentum transfer of photon i due to scattering inside the medium. In the baseline state, we ignore the presence of directed blood flow and assume that the flow can be modeled as a Brownian motion, i.e., $\langle \Delta r^2(\tau) \rangle = 6D_B \tau$. For a small perturbation at a voxel location \mathbf{r}_j in the form of directed flow introduced inside the tissue medium, and assuming the

photon paths remain exactly the same, the change in speckle contrast at voxel location \mathbf{r}_d and light source location \mathbf{r}_s is given by $\Delta K^2(\mathbf{r}_d, \mathbf{r}_s)$, where,

$$\begin{aligned}\Delta K^2(\mathbf{r}_d, \mathbf{r}_s) &= \frac{2\beta}{T} \int_0^T \left(1 - \frac{\tau}{T}\right) [g_1'^2(\mathbf{r}_d, \mathbf{r}_s, \tau) - g_1^2(\mathbf{r}_d, \mathbf{r}_s, \tau)] d\tau, \\ &= \frac{2\beta}{T} \int_0^T \left(1 - \frac{\tau}{T}\right) [g_1'(\mathbf{r}_d, \mathbf{r}_s, \tau) - g_1(\mathbf{r}_d, \mathbf{r}_s, \tau)][g_1'(\mathbf{r}_d, \mathbf{r}_s, \tau) + g_1(\mathbf{r}_d, \mathbf{r}_s, \tau)] d\tau,\end{aligned}\quad (10)$$

where $g_1'(r)$ denotes the new normalized field autocorrelation function at pixel location \mathbf{r}_d due to perturbation at a voxel location \mathbf{r}_j in the medium. Assuming the change in perturbation is really small, Eq. (9) can be used to simplify the expression in Eq. (10), given by,

$$\Delta K^2(\mathbf{r}_d, \mathbf{r}_s, \mathbf{r}_j) = -\frac{4\beta k_0^2}{3T} \int_0^T \left(1 - \frac{\tau}{T}\right) g_1(\mathbf{r}_d, \mathbf{r}_s, \tau) \sum_i w_i'(\tau) Y_i(\mathbf{r}_j) \delta V^2(\mathbf{r}_j) \tau^2 d\tau, \quad (11)$$

where $Y_i(\mathbf{r}_j)$ is the momentum transfer of i^{th} photon in the voxel located at \mathbf{r}_j , $w_i'(\tau) = w_i \exp[2k_0^2 D_B \tau \mu_s' L_i]$ is the modified weight for the i^{th} photon packet, and D_B is the baseline blood flow. We can write a similar expression for the reduced speckle contrast corresponding to perturbation in any voxel location in the medium, given as,

$$\Delta K^2(\mathbf{r}_d, \mathbf{r}_s) = -\frac{4\beta k_0^2}{3T} \sum_{\mathbf{r}_j} W_m(\mathbf{r}_d, \mathbf{r}_s, \mathbf{r}_j) \delta V^2(\mathbf{r}_j), \quad (12)$$

where,

$$W_m(\mathbf{r}_d, \mathbf{r}_s, \mathbf{r}_j) = \int_0^T \left(1 - \frac{\tau}{T}\right) g_1(\mathbf{r}_d, \mathbf{r}_s, \tau) \sum_i w_i'(\tau) Y_i(\mathbf{r}_j) \tau^2 d\tau. \quad (13)$$

For a particular source-detector configuration setup in MCX, the simulation output returns $w_i'(\tau)$ for a particular value of temporal parameter τ . The process of obtaining $w_i' Y_i$ is explained in more detail in the next section. The sensitivity matrix is formed by generating W_m for different source and detector locations \mathbf{r}_s and \mathbf{r}_d . There are two main factors to consider here. Firstly, generating the sensitivity matrix requires computation of $w_i'(\tau) Y_i$ for different correlation times $\tau \in (0, T)$. If we uniformly sample N_t points in $(0, T)$, then we need to run the simulation N_t times for a particular configuration. Secondly, multiple configurations of sources and detectors are needed to obtain dense measurements for high-resolution tomographic reconstruction. Since each camera pixel acts as a separate detector, a single light source position corresponds to thousands of individual measurements. Generating the sensitivity matrix values for each detector position is practically infeasible.

4. Proposed method: SpeckleCam

In this work, we propose to solve the computational challenge in generating the sensitivity matrix values using two key subparts-i) photon replay approach to building the sensitivity matrix for different correlation time τ , and ii) a convolution-based forward model that helps us build an efficient reconstruction problem based on the forward model.

4.1. Generating the sensitivity matrix via photon replay method

The sensitivity matrix generation involves computing the photon weights w_i' dropped at each voxel location \mathbf{r}_j within the medium during propagation for each correlation time τ , as in (12) and (13). The MCX simulation starts with launching many photons at the source location, and the scattering events and the path trajectory are stored for all the photons reaching the detector. A key

consideration is that with changing correlation time τ , the scattering coefficient of the medium remains constant; hence the scattering events and the path trajectory is independent of τ . We can then employ the photon replay approach [33], inspired by the "reseeded" perturbation-based Monte Carlo method proposed in [34]. The photon-replay method has been used in building the sensitivity for hyperspectral imaging for diffuse optical tomography applications [33]. The photon replay approach starts with a baseline simulation where a large number of photons are launched with initial seeds generated with a deterministic pseudorandom number generator. Some photons are detected at the detector location, and the corresponding photon seeds, photon trajectory, and photon weights w'_i are recorded. Subsequent simulations, known as the photon replays, launch the photons initialized with saved photons seeds and weights w'_i , thereby guaranteeing that the photons follow the same trajectory and are detected at the exact same position as the baseline simulation. During re-propagation, the photon weights w'_i are used to compute weighted momentum transfer $w'_i Y_i$ at each voxel location \mathbf{r}_j , which is then summed up for all the detected photons at \mathbf{r}_j . For different τ values, we recalculate the weights $w'_i(\tau)$ and repeat the photon trajectory by "replaying" without the need to re-run the baseline simulation. Running the baseline simulation is the main computational bottleneck, and the computation time is directly related to the number of launched photons (typically in orders of 10^8). We save computation time significantly by avoiding the need to run the baseline simulation repeatedly for different τ values. Specifically, if we use $N_t = 20$ values for $\tau \in (0, T)$, we achieve a speedup of 20 \times using the replay method.

4.2. Convolution approximation

Next, we need to generate the sensitivity W_m for different source-detector configurations. Computing the sensitivity for many detectors will take thousands of hours and is practically infeasible using the traditional Monte Carlo approach. To solve the infeasibility problem, we generate the sensitivity matrix by keeping the detector fixed at the center of the scattering medium surface and changing only the line source's position. In our system, we use a horizontal slit line source instead of a point source and scan the line source vertically across the surface of a sample. We use our system geometry to set up the Monte Carlo simulation configuration in MCX.

For our setup, we show examples of the generated sensitivity matrix by changing the location of the line source and the pixel detector, shown in Fig. 3. The sensitivity matrix has a *banana-shaped* path that is similar to the one obtained for Diffuse Optical Tomography (DOT), except that the matrix in DOT is derived for absorptive contrast. In contrast, in speckle contrast tomography, the matrix is obtained for contrast in the flow of scattering particles. The sensitivity matrix values directly depend on the source and detector locations. Let us denote the vertical distance between the midpoint of the line source and the detector as the source-detector distance. From instances of the generated sensitivity matrix, we observe that as the distance between the source and the detector increases, the deeper voxels in the sensitivity matrix have higher values. Therefore the speckle contrast change is more sensitive to changes in flow from deeper layers. Also, the sensitivity values decrease rapidly as we consider voxels very far away from the source or detector for a particular configuration. Secondly, we note an essential property of the sensitivity for a fixed exposure time. From Fig. 3, we observe that the sensitive matrix is spatially invariant. Assuming the line source length is long enough, the sensitivity matrix has the same blur profile. Moreover, the blur profile depends only on the distance between the detector and the midpoint of the line source, and we denote this distance as $y_{sd} = y_s - y_d$, where y_s and y_d are the y-coordinate of the source and the detector location respectively, as shown in Fig. 3. Hence, we can define W_m as a function of relative voxel location in a particular source-detector configuration than absolute voxel locations. Specifically, we replace $W_m(\mathbf{r}_d, \mathbf{r}_s, \mathbf{r}_j)$ with a kernel $\kappa_m(\mathbf{r}_j - \mathbf{r}_d, \mathbf{r}_s - \mathbf{r}_d)$. Inspired by the similarity in the DOT-based sensitivity matrix [35], the spatial invariance property of the kernel can then be used to replace the matrix multiplication expression in Eq. (13) with a

convolutional form, given as,

$$\Delta K^2(\mathbf{r}_d, y_{sd}) = -\frac{4\beta}{T} \kappa_m(y_{sd}, \mathbf{r}_d) \otimes \delta V^2(\mathbf{r}_d), \quad (14)$$

where $\delta V^2(\mathbf{r}_d)$ is the 3D blood flow values that we want to recover, $\mathbf{r}_s - \mathbf{r}_d = y_{sd}$, and the operator \otimes denotes the depth-wise convolution.

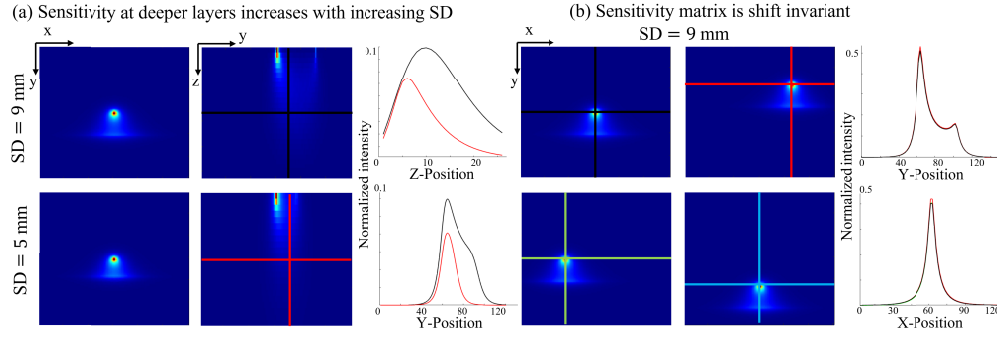


Fig. 3. We show examples of the generated sensitivity matrix at different source-detector locations. (a) The sensitivity matrix is dependent on source-detector separation distance SD. The sensitivity for deeper layers increases with a larger source-detector distance. (b) The sensitivity matrix is shift invariant; the blur profile only depends on the source-detector distance SD and is independent of the absolute detector location. We use this property to formulate our convolution-based forward model.

In our setup, a camera records images for different line source positions \mathbf{r}_s . The speckle contrast images are obtained for each image resulting in a 3D set of images $K^2(\mathbf{r}_d, \mathbf{r}_s)$, where $\mathbf{r}_d \Rightarrow (x, y)$ denotes the speckle contrast at pixel location (x, y) for a line source located at \mathbf{r}_s . We transform the 3D set of images $K^2(\mathbf{r}_d, \mathbf{r}_s)$ to $K^2(\mathbf{r}_d, y_{sd})$, such that each speckle contrast value at location \mathbf{r}_d in an image now corresponds to a constant source-detector separation distance y_{sd} .

Using a convolutional forward model, we mainly bypass the computational complexity associated with the matrix inversion step.

4.3. Reconstruction algorithm

Given a set of images $K^2(\mathbf{r}_d, y_{sd})$, we want to recover the 3D blood flow maps. We first subtract the baseline flow $K_0^2(\mathbf{r}_d, y_{sd})$ from the speckle contrast measurements to obtain $\Delta K^2(\mathbf{r}_d, y_{sd})$. Using our forward model, we estimate the blood flow map using the following optimization problem,

$$\min_Q \sum_{y_{sd}=y_{sdmin}}^{y_{sdmax}} \|\Delta K^2(y_{sd}) - \kappa_m(y_{sd}) * Q\|_F^2 + \lambda \|Q\|_1, \quad (15)$$

where $\|\cdot\|_F$ denotes the Frobenius norm, $\|\cdot\|_1$ denotes the l_1 norm and Q represents the change in blood flow δV^2 in three dimension, $\Delta D_B(\mathbf{r}_d)$. We assume that the change in blood flow is spatially sparse; hence we add a sparsity-based regularizer on Q to constrain the solution. For very small y_{sd} , the pixels are located very close to the line source and might be saturated. Moreover, the diffusion approximation breaks down for very small source-detector distances. On the other hand, pixels located far from the source receive very few backscattered photons and are mostly dominated by the camera sensor noise. Hence we chose an optimal range of y_{sd} from $y_{sdmin} = 2.5$ mm to $y_{sdmax} = 14$ mm for the optimization problem in Eq. (15).

With the reconstruction algorithm in Eq. (15), we achieve better performance than the state-of-the-art reconstruction methods. Firstly, the formulated reconstruction algorithm is more memory

efficient than the traditional matrix inversion-based algorithms. Secondly, the generated sensitivity kernel κ_m is more accurate (as shown in subsection 6.1.2) than a diffusion approximation-based matrix. One might argue that Monte-Carlo simulations are slower and computationally intensive than the diffusion approximations-based model. However, generating the matrix is a one-time computation for a known range of human tissue parameters, and can be computed beforehand.

5. Hardware

This section discusses our experimental setup and data collection methods for tissue-mimicking phantom and in vivo experiments on human subjects.

Our experimental setup is shown in Fig. 4. We use a continuous wave line laser (model: STR 785 100 HR-L01-5-S), with a maximum power of 100 mW and 785nm wavelength with a fan angle of 5 degrees to project a line instead of a point source. We then place a pair of galvo mirrors (ThorLabs GVS012) to direct the laser beam onto the surface of the scattering medium. The line beam was focused to a line (length < 5 cm, width < 1mm) at a distance of 50 cm from the laser diode. The laser was operated at a power of 70 mW, which is well below the safety limit for human tissue. For a detector, we use a CMOS camera (Oryx, model: ORX-10GS-51S5M-C: 5.0 MP, 162 FPS, Sony IMX250) in reflection mode to record images in reflection geometry. We use the cross-polarization technique to reject direct surface reflection from the surface of the medium. A polarizing filter is used in front of the camera lens and is oriented perpendicular to the polarizing direction of the laser source. For all experiments, we set the camera aperture diameter at $f\# = 4$ so that the speckle size roughly matches the pixel size of the camera sensor. The camera's field of view is 3 cm \times 3 cm, and we operate the camera at 400 frames per second.

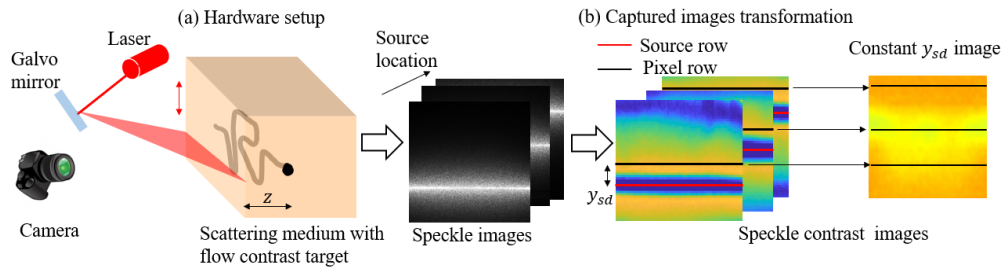


Fig. 4. The schematic of our hardware setup for data collection and data transformation for obtaining constant source-detector separation images. (a) We use a pair of galvo mirrors to scan a line source on the surface of the scattering medium. The target is a structured hollow pipe at $z = 6$ mm from the surface, and a pump maintains a constant flow of scattering particles through the pipe. (b) Each image corresponds to a location of the light source. The images are then transformed to form a constant source-detector distance y_{sd} images, which are used for fitting our convolution-based forward model.

The galvo-mirror is synchronized with the camera such that the camera acquires frames for each position of the light source as determined by the galvo mirror. We use a camera exposure time of 0.5 ms to make our setup more sensitive to faster flow speed inside the medium. We scan the sample in one direction along $N_s = 30$ horizontal light source positions arranged uniformly on the sample's surface. The total scanning time is 15 seconds.

We capture images at a spatial resolution of 800×800 . The speckle contrast is calculated based on a spatial filter with 11×11 pixel neighborhood for each image. We then average the speckle contrast across 100 images to reduce the effects of noise, resulting in a single speckle image for each line source position. We perform a shot-noise correction on the speckle contrast, similar to the method described in [25]. The speckle images are further downsampled by a factor of 8, resulting in a 3D stack of speckle contrast images $K^2 \in \mathbb{R}^{100 \times 100 \times N_s}$, where N_s corresponds

to the total number of source locations ($N_s = 30$). We then perform a grid-based transformation $K^2(x, y, y_s) \Rightarrow K^2(x, y, y_s - y)$, shown in Fig. 4 such that each speckle contrast value in an image $K^2(x, y, y_{sd})$ now corresponds to a constant source-detector pair distance y_{sd} .

6. Experiments and results

This section shows our results on recovering deep-flow images at a high resolution. Using our approach, the estimated blood volume map is a 3-dimensional voxel grid of $100 \times 100 \times 33$ voxels corresponding to a volume of $30 \times 30 \times 10 \text{ mm}^3$. We implement a prior method [25] which involves a matrix inversion-based reconstruction algorithm for comparison. For the prior method, we estimated the blood flow map corresponding to the same volume but divided into $32 \times 32 \times 8$ voxel grid to keep the memory requirements comparable for both methods. We perform extensive experiments using dynamic tissue phantoms and human subjects to validate our system.

6.1. Tissue phantom experiments

A tissue phantom enables us to test our system under different controllable parameters. We discuss how we build complex tissue phantoms mimicking human tissue and blood vessels, and then describe the performance of our system SpeckleCam.

6.1.1. Building a dynamic tissue phantom

We build dynamic tissue phantoms to mimic human tissue and major blood vessels deep inside the tissue. Our goal is to test the resolution of the system in reconstructing deep flow maps. As the homogeneous scattering medium, we use milk solution with 1% fat content in a cube ($5 \text{ cm} \times 5 \text{ cm} \times 5 \text{ cm}$). The scattering and absorption coefficient was estimated to be $\mu_s = 6.5 \text{ mm}^{-1}$ and $\mu_a = 0.0015 \text{ mm}^{-1}$ using time domain spectrometry as described in [36]. The scattering coefficient is in agreement with the actual scattering property of the human tissue. Using the estimated optical properties, we fit speckle contrast profiles at different distances from the light source, and the diffusion coefficient was estimated to be $D_B = 1.5 \times 10^{-6} \text{ mm}^2/\text{s}$. For perturbation, we 3D printed hollow pipes with an inner diameter of 1 mm and different shapes with clear transparent walls. We place the tubes at 6 mm from the surface of the scattering medium, corresponding to ≈ 40 mean free paths (MFPs). We then use the same milk solution [37] to pass through the tube using a syringe pump (New Era 4041) at various flow speeds, although an intralipid solution [38] can be also used to mimic blood in tissue phantoms.

6.1.2. Phantom results

Diffusion-based vs. Monte Carlo-based model. In order to evaluate the quality of depth reconstruction, we design the target to have features at variable depths. Specifically, we use two targets, the first one is an 'S' shape kept slanted along the depth, and the second target consists of 'U' and 'S' shapes located at 3 and 5 mm, respectively. We pump fluid through the hollow pipes at a speed of 1 cm/s. The flow speed is chosen in accordance with the actual blood flow in major blood vessels like the veins and the arteries. We demonstrate the results of depth reconstruction using the Monte Carlo-based forward model and compare it with the traditional diffusion-based model, as shown in Fig. 5. This is because the diffusion-based method has very poor accuracy in the shallower layers. The superficial features dominate the deeper features in the reconstructed process; hence results in a poor reconstruction quality of the deeper features. On the other hand, the Monte Carlo-based matrix performs better at recovering the deep features, and the reconstruction is closer to the ground truth. Additionally, we show slices from the reconstructed volume from the Monte Carlo-based approach. The slices from the reconstructed volume at variable depths reveal depth-sensitive features.

Resolution experiments. We show examples of reconstruction on complicated structures 6 mm deep from the surface of the medium in Fig. (6). We show the difference in speckle contrast

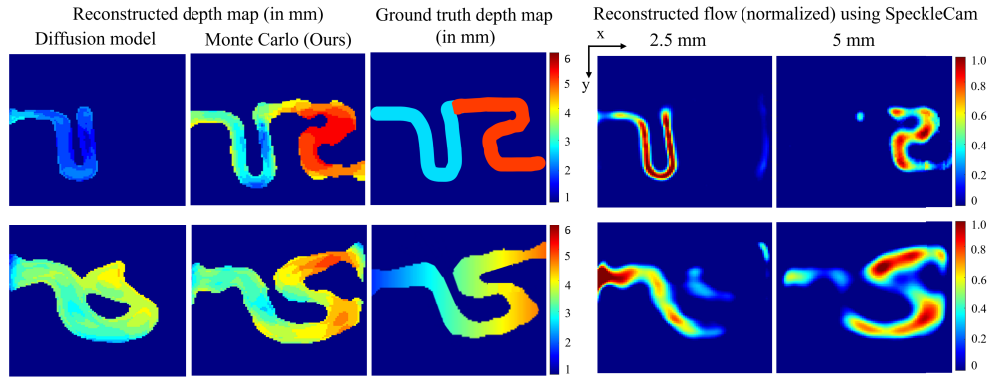


Fig. 5. Examples of depth reconstruction using our (Monte Carlo-based) approach vs. traditional diffusion-based forward model. The targets are designed to have two different structures at variable depths inside the medium. The top row corresponds to a structure that consists of two features, 'U' and 'S' shapes, at two distinct depths. The bottom row has the 'S' shape structure kept slanted along the depth. The colormap in the left half of the image provides the depth scale. The depth map from the diffusion-based sensitivity matrix cannot recover the full structure from the medium, compared to the Monte Carlo-based sensitivity matrix. The slices from the reconstructed volume from two different depths demonstrate that our approach can recover the features successfully.

images from the baseline flow, $\Delta K^2(\mathbf{r}_d, y_{sd})$ for a source-detector separation $y_{sd} = 3$ mm. The camera measurements record the spatial change in flow; however, the images are blurred due to light scattering, and the original target cannot be discerned in the measurements alone. We use our approach to reconstruct the blood flow volume, and we show a slice at a depth of 6 mm in the reconstructed volume. SpeckleCam can recover the structure in high resolution compared to the prior work. To test the spatial resolution achieved with our setup, we use a target consisting of two pipes with 1 mm diameter and 2 mm separation between the pipe boundaries. From the reconstructed slice, we see that SpeckleCam can clearly resolve the two lines. Overall, SpeckleCam improves the spatial resolution by $3\times$ at a depth of 6 mm over the low-resolution prior work.

Sensitivity experiment. We also test the sensitivity of our system by varying the flow speeds in the dynamic tissue phantom. The reconstructed slice using a sensitivity matrix derived from both diffusion approximation and Monte Carlo simulation is shown in Fig. 7 for various flow speeds. With decreasing flow speed, the difference in contrast signal in the speckle contrast image gets weaker, and the camera measurements are mostly dominated by noise. As a result, the quality of the reconstruction result is expected to decrease for lower flow speeds. We observe that the reconstruction quality is slightly better for Monte Carlo-based sensitivity matrix over diffusion approximation (not shown here), with the reconstruction parameters remaining the same in both methods. Our system is capable of detecting structures with flow speeds as low as 5 mm/s.

6.2. In vivo experiments

We also perform human experiments to validate how well SpeckleCam translates to real data. We describe our experimental protocols and results next.

6.2.1. Methodology

We validate our system's sensitivity to human subjects' blood flow changes. A manual pressure cuff is generally used for occluding the arm to induce variations in blood flow [11,39]. We

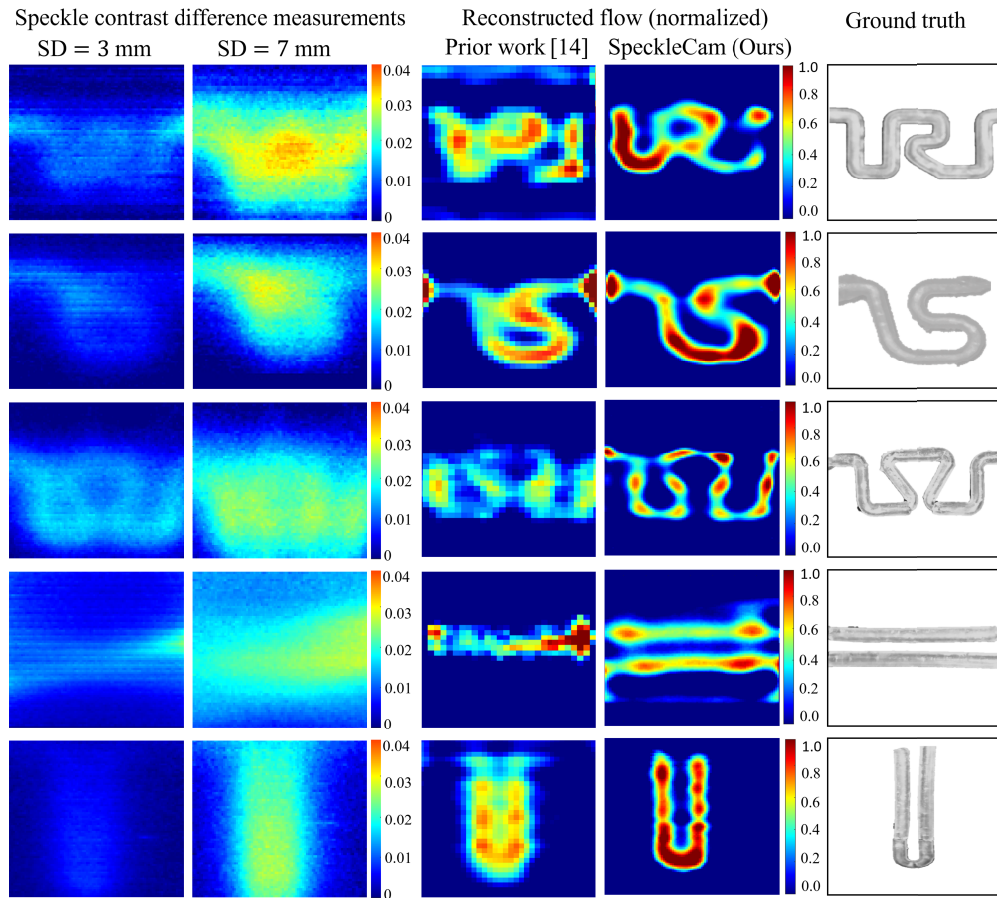


Fig. 6. Examples of results on simulated data. All the targets are kept at a depth of 6 mm from the surface of the scattering medium. We show a slice from the reconstructed blood flow map using our approach. We show we can recover flow in high resolution compared to matrix-inversion-based reconstruction methods. The structure of the pipe, which serves as the ground truth, is shown in the rightmost column.

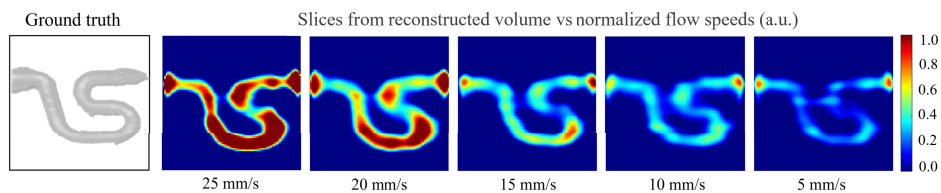


Fig. 7. Examples of flow reconstruction with various flow speeds. The reconstruction quality degrades as we decrease the flow speed, but our approach can recover structures with flow speeds as low as 5 mm/s.

recruit 5 subjects for the study, where we image the arm and wrist regions while occluding the upper arm region at different occlusion pressure. The experimental protocol was approved by the Rice University Institutional Review Board (Study number: IRB-FY2023-59, Approval Date: 19/01/2014). The blood flow is inversely proportional to the occlusion pressure, and we test our system to image blood flow in veins at different occlusion pressure. For each region, we apply occlusion pressure for 30 seconds and collect images 10 seconds after the start of occlusion, followed by 30 seconds of no occlusion where no data is being recorded. After the no occlusion period, we raise the occlusion pressure and collect images. We follow the same protocol and collect data corresponding to 0, 30, 60, 90 and 140 mm Hg. The images correspond to 3 occlusion stages of 0, 30 and 60 mm Hg. For optical properties of the human arm, we use scattering coefficient $\mu_s = 5.68 \text{ mm}^{-1}$ and absorption coefficient $\mu_a = 0.011 \text{ mm}^{-1}$ as estimated in [40]. Blood in arteries and veins flows at a high speed, in the order of centimeters per second, as opposed to capillaries where the blood flow speed is in millimeters per second. Since we are interested in recovering flow speed in deeper blood vessels like arteries and veins, we image regions with a low camera exposure time of 0.75 milliseconds.

6.2.2. In vivo results

Model fitting. With occlusion pressure, the blood flow in the tissue gets affected. The mean particle displacement, hence the diffusion coefficient D_B , should decrease with increasing occlusion pressure. To validate this, we estimate D_B by using the model in Eq. (3) for various occlusion pressures. The measured data consists of a 3D stack of speckle contrast image measurements for each occlusion pressure. The speckle contrast at a pixel reduces with increasing distance from the source for known tissue optical properties. We choose a small region of the tissue devoid of major blood vessels. In the small region, the contrast fall-off profile with increasing source-detector distance is then used for fitting the model with respect to D_B . We choose the source-detector distance in the range of 5 mm and 15 mm for fitting the model. Pixels located less than 5 mm from the source line are mostly saturated. On the other hand, pixels located further than 15 mm are corrupted with noise since the pixels receive very few photons. Therefore we use a suitable range between 5 mm and 15 mm for estimating the particle diffusion coefficient D_B . Speckle contrast computed at a detector decreases with increasing source-detector distance and increasing blood flow speed for a fixed camera exposure time, as shown in Fig. 8. We plot the variation of normalized speckle contrast for a range of source-detector distances. We observe that the normalized speckle contrast curve decays faster at lower occlusion pressure. Low occlusion pressure allows higher blood flow in the tissue, and hence the speckle contrast decreases more rapidly. At higher occlusion pressure, there is limited blood flow, and hence the normalized speckle contrast decays slowly with increasing source-detector distance. We show that the model-predicted speckle contrast values match the experimental values. The estimated D_B are $3.9 \times 10^{-7} \text{ mm}^2/\text{s}$ for 0 mm Hg, $2.64 \times 10^{-7} \text{ mm}^2/\text{s}$ for 30 mm Hg and $0.68 \times 10^{-7} \text{ mm}^2/\text{s}$ for 60 mm Hg. The overall D_B decreases with increasing pressure and is expected since increasing occlusion pressure reduces tissue blood flow.

Imaging. The inverse model requires baseline contrast images for reconstruction. The baseline contrast images can be generated apriori for a known set of tissue parameters. In this work, we consider the images at 140 mm Hg to be the baseline when there is no blood flow in the tissue. We then subtract the baseline contrast images from the contrast images at other occlusion pressures, thereby obtaining ΔK^2 for occlusion pressures at 0, 30, 60, and 90 mm Hg. We use each set of ΔK^2 as measurement input to our SpeckleCam reconstruction approach. We show some of the difference contrast images ΔK^2 and the reconstruction result using our proposed approach, SpeckleCam, in Fig. 9. We note two key observations. Firstly, the slice at a depth of 2 mm from the reconstructed volume has an improved spatial resolution over the contrast images. The improved resolution is evident from the zoomed insets and the corresponding line profiles, which

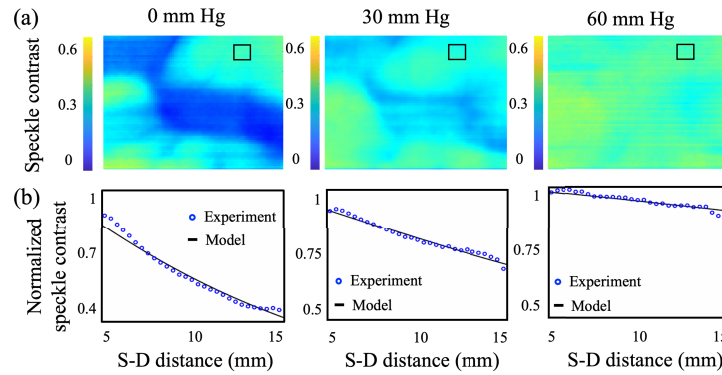


Fig. 8. The speckle contrast decays with increasing source-detector separation. With the optical properties of the medium assumed to be constant, the decay depends on the mean particle displacement. We show the speckle contrast image (top row) and noise-corrected normalized speckle contrast (in the black square) for different occlusion pressure. With increasing occlusion pressure, the speckle contrast decays slowly due to decreasing speed of the blood cells inside the tissue. The estimated diffusion coefficients D_B are 3.9×10^{-7} mm²/s for 0 mm Hg, 2.64×10^{-7} mm²/s for 30 mm Hg and 0.68×10^{-7} mm²/s for 60 mm Hg.

show relatively sharper structures of the blood vessels in the reconstructed slices. Secondly, we observe that the blood flow in different vessels decreases at a different rate with the increasing occlusion pressure. The difference in blood flow may be due to the underlying physiology and can be explored further to provide useful clinical diagnoses. We also show some more examples of speckle contrast images, intensity images, and the reconstruction result using SpeckleCam in Fig. 10. The intensity images and the speckle contrast images correspond to a source-pixel distance $y_{sd} = 6$ mm. The intensity images are shown only for visualization purposes and are not used in the reconstruction pipeline. The intensity change in pixel on a major blood vessel due to occlusion pressure is negligible. The pixel intensity depends mainly on the concentration of the absorbing element. During occlusion, there is only a slight change in blood volume in the vessel; hence the pixel intensity change is not noticeable. However, increasing the occlusion pressure reduces the blood flow; hence the speckle contrast changes due to occlusion pressure. Although the difference in contrast images from the baseline reflects the change in contrast due to occlusion, the size or diameter of the blood vessel is not prominent, as light scattering results in low spatial resolution of the captured images. Using our reconstruction pipeline, we use the speckle contrast images to recover deep blood flow in high resolution. In the reconstructed blood flow map, the flow in the major vessel decreases with increasing occlusion pressure for all the examples shown. For occlusion pressure of 60 mm Hg, the blood flow signal is weak, and hence the reconstruction fails to recover any discernable structure of the blood vessel. Finally, 90 mm occlusion pressure totally occludes the blood flow in the imaged veins. In our vivo experiments, we do not have the ground truth of the blood vessels. The absence of any ground truth makes it difficult for us to compare and analyze the depth variation of the reconstructed blood vessel, which might be important in certain applications [41]. Therefore, we mainly highlight the blood flow changes at depth slices where the estimated flow is dominant in the reconstruction volume.

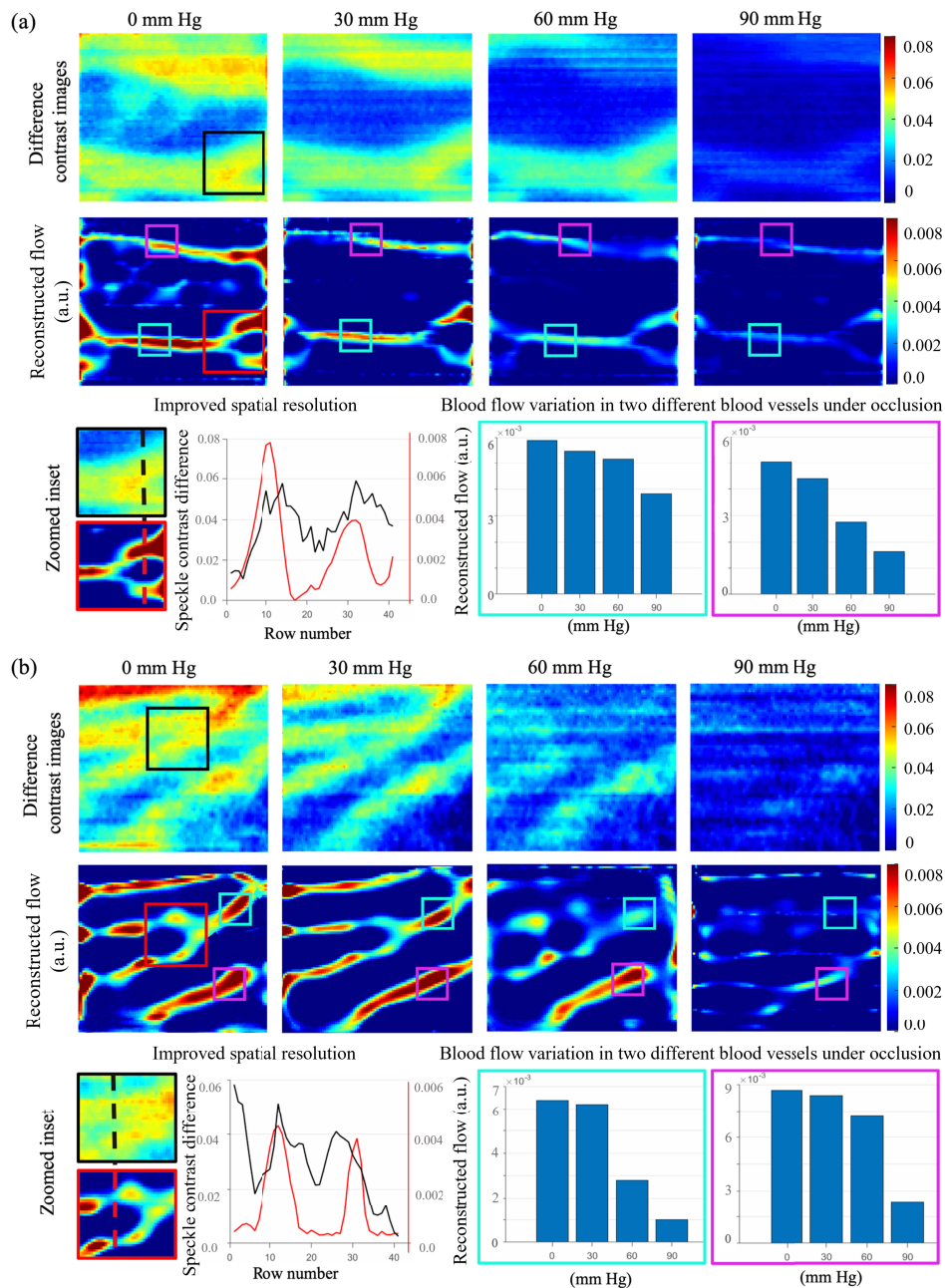


Fig. 9. Examples of results from in vivo experiments under different occlusion pressure. The difference in contrast images from baseline (top row) and reconstructed slice (second row) using SpeckleCam are shown. The reconstructed slice has improved spatial resolution over the simple speckle contrast images, as evident from the zoomed insets. We also capture different rates of decreasing blood flow in two different blood vessels (shown in magenta and cyan squares) with increasing occlusion pressure.

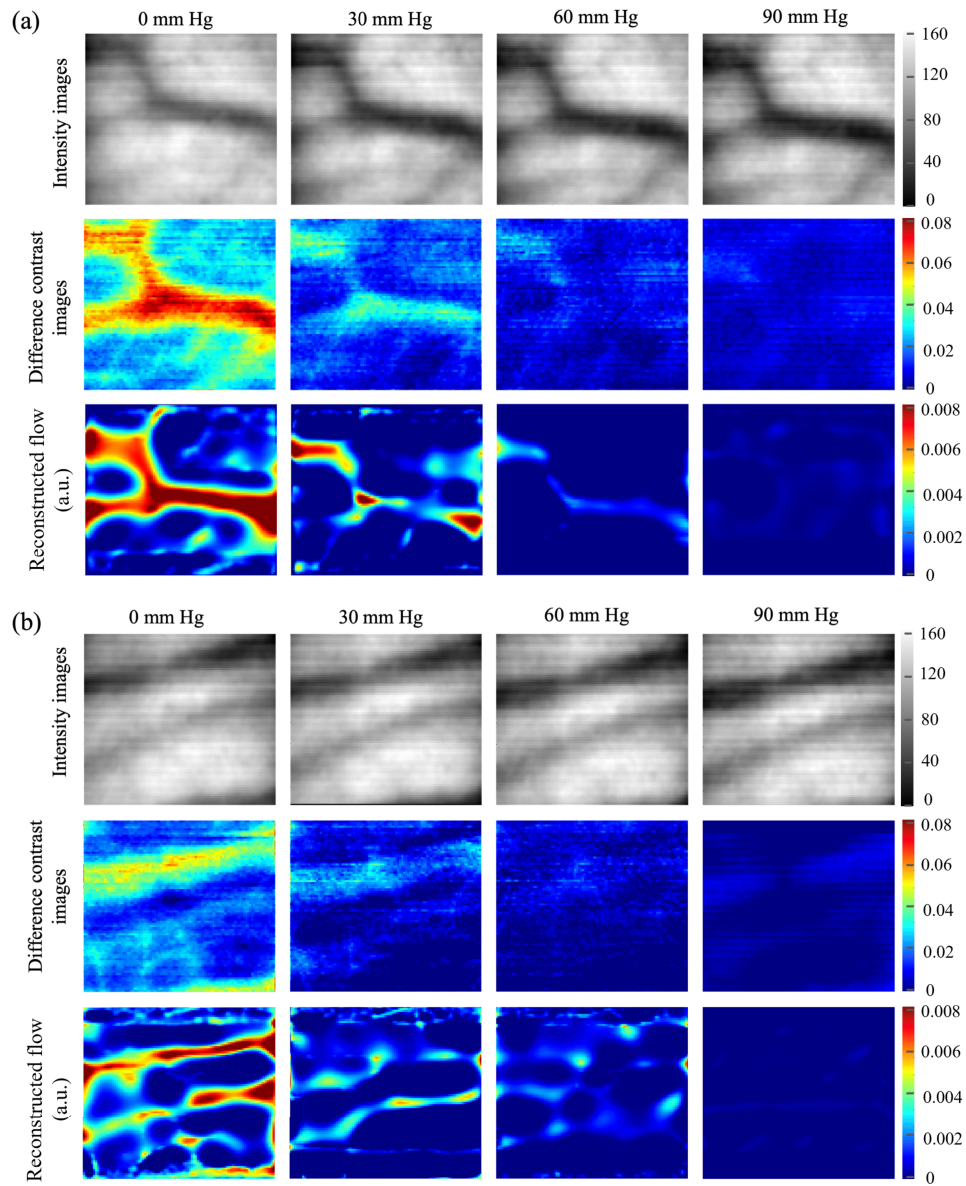


Fig. 10. Examples of reconstruction results from in vivo experiments under different occlusion pressure. We image two regions on the arm. The intensity images (top row), the difference speckle contrast images from the baseline (second row), and the reconstruction slice (third row) are shown. The intensity images do not change significantly on applying occlusion pressure since there is only a slight change in the blood volume. The speckle contrast image is sensitive to blood flow, for 60 mm Hg occlusion pressure, there is no flow contrast in the region of the big blood vessel. However, light scattering results in the blurring of speckle contrast images. SpeckleCam recovers the blood flow map in high spatial resolution.

7. Discussion and conclusion

We have presented SpeckleCam for deep tissue blood flow imaging in high resolution. In this section, we discuss several aspects of our proposed technology and some future directions which may improve the performance of our current approach.

Computational runtime. For the traditional method, the reconstruction time is 30 seconds for reconstructing a flow volume consisting of $32 \times 32 \times 8$ voxels, and more than 8 minutes for $48 \times 48 \times 12$ voxels. The computation time and memory allocation scale up exponentially with the increasing dimensions of the sensitivity matrix. For SpeckleCam, the reconstruction time is less than 2 minutes for 500 iterations for reconstructing the blood flow volume consisting of $100 \times 100 \times 32$ voxels, and less than 5 minutes for $200 \times 200 \times 64$ voxels.

Speckle size. It has been reported in [42] there is a slight intensity function distortion when the speckle size is less than 2 times the pixel size, with around 20% reduction in speckle contrast when the speckle size matches the pixel size. However, there is a tradeoff to be considered when choosing the speckle size for imaging. There are two main ways to increase speckle size, by using longer wavelength and by using higher $f\#$. Using longer wavelengths increases penetration depth, but the camera sensitivity decreases for longer wavelengths. Secondly, increasing $f\#$ reduces the aperture diameter of the camera lens, thereby reducing the light captured at each pixel. Reduced camera sensitivity and low image brightness increase dark noise in the acquired images, specifically at larger source-detector distances for fixed laser power. Therefore increasing the speckle size comes at the expense of increased noise in measurements. Hence, we match the speckle size to pixel size according to [25] to obtain an optimal set of measurements.

Sparsity regularizer. An optical tomography reconstruction is an ill-posed problem. Hence regularizers are commonly used to constrain the solution space. Generally, a sparsity regularizer is used when the target is known to be sparse in the reconstruction volume. In this work, the regularizer weight is chosen manually based on the quality of the reconstruction. The comparison of SpeckleCam with the prior method for a single phantom is shown in Fig. 11. The sparsity regularizer helps in resolving spatially close structures in the reconstructed flow image. While the reconstruction results using the traditional method improve with sparsity regularizer, however, the quality is much inferior to SpeckleCam in the ability to resolve finer structures.

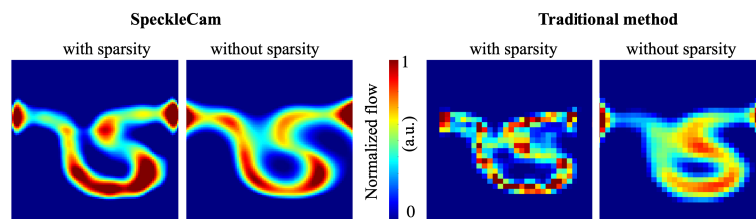


Fig. 11. We show the impact of sparsity-based regularizer on the reconstruction results for both SpeckleCam and traditional methods. Sparsity regularizer in SpeckleCam helps in resolving finer structures better than the traditional methods.

Validity of the small flow perturbation assumption from the baseline. In this work, we assume that the change in flow perturbation is small compared to the baseline for developing the forward model. However, in cases where there is a large change in blood flow, this assumption might not be valid. There are two main factors for consideration here. First, the background signal arises from the smaller blood vessels with blood speed < 1 cm/sec. The sensitivity of a speckle contrast imaging system can be controlled by the camera exposure duration. Therefore, to suppress the background signals, we have used a very low camera exposure duration of 0.75 ms. The exposure duration is chosen such that our system is mostly sensitive to larger blood vessels with higher blood flow speeds. Therefore, the change in background signal is relatively less when compared

to the baseline. Secondly, reconstructed blood flow follows a linear response with changes in actual blood flow speed at lower speed differences. However, a large change in the flow speed introduces a non-linear response in the reconstructed blood flow as shown in [25]. The sensitivity of the system decreases at larger flow speeds. This is a known problem in optical tomographic reconstructions. A solution can be to compute a response curve of estimated blood flow vs. actual blood flow via experiments. This response curve can be used to deduce the actual blood flow when deployed in real applications. Furthermore, capturing measurements with multiple exposure times can further improve flow speed estimation.

Ordered motion vs. shear-induced diffusive motion. Blood flow can be quantified well with a hybrid model describing both Brownian motion (from diffusive flow arising from shear stress) and advective motion (directed flow) [43]. The speckle contrast depends on a combination of both types of motion. The problem of separating the contributions from both the above-mentioned factors is well-studied and characterized [44,45]. In [46,47], the authors have reported the contribution from shear-induced diffusion decreases with increasing vessel diameter and flow speeds, and the contribution from ordered flow significantly dominates at the baseline conditions (for no occlusion) that we consider in this work. However, at higher occlusion pressure, the shear-induced diffusion increases and might introduce error in the estimated blood flow speed. To account for the modeling error, both diffusive and ordered motion should be considered in the forward model and this will guide our future efforts to improve the accuracy of SpeckleCam.

Generating the sensitivity kernel. The generation of kernel κ_m in (14) relies on the perturbation approach based on Monte Carlo simulations, and is prone to noise. To reduce the effects of stochastic noise, a sufficient number of photons need to be used in the simulation, or multiple simulation runs need to be averaged, both of which increase the computational complexity to some extent. Instead, several post-processing filtering techniques [33] help in improving the accuracy of the generated kernel. Generating the sensitivity matrix involves only a one-time computation for a known range of human tissue properties, and hence can be computed apriori. Secondly, we observe that the quality of the depth reconstruction deteriorates with increasing spatial overlap in the features located at variable depths. The contrast signal from the shallower features dominates the deeper features, and it becomes increasingly difficult to separate features with considerable $x - y$ plane overlap between them. One primary reason is that the sensitivity values decrease exponentially with increased depth from the scattering medium surface. To tackle this issue of reduced sensitivity at deeper levels, a depth-compensated weighted sensitivity matrix [48,49] has been shown to be useful in optical tomography applications and can be adapted to our pipeline as well.

Data acquisition time. In this work, we assume the flow to be stationary during the scan time. However, various clinical applications involve imaging dynamic blood flow changes, and the imaging setup has to be suited to the time scale of the blood flow fluctuations. For example, a real-time blood flow imaging setup (10-100 fps) might be necessary for applications like perfusion monitoring during cerebrovascular surgery [50,51], and flow pulsatility imaging for vascular health monitoring [52,53]. Secondly, in applications like burnt wound monitoring, and anesthetic onset measurement [54], blood flow changes occur in minute scale and this allows the use of a relatively slower (0.1-1 fps) imaging setup. Thirdly, in applications like wound healing monitoring, deep tissue flow estimation for diagnosing peripheral arterial diseases, and dermatological applications, the blood flow can be considered to be stationary. The current SpeckleCam system with a scanning time of around 15 seconds, can be used in the third category of clinical applications. Hardware improvements like using a faster camera with sensitive sensors (EMCCD) will further reduce the scanning time with the same performance. For example, using a 1000 FPS camera will further reduce the scanning time by 3 times, thereby allowing SpeckleCam to be useful in some of the applications like wound monitoring and assessment. For faster flow changes, for example, while imaging blood flow pulsatility, the flow estimated by

SpeckleCam is an average flow during the scanning interval. The acquisition time in SpeckleCam and many similar scanning-based systems [15,25], is, therefore, a bottleneck towards application in real-time in vivo imaging.

In conclusion, we have developed and demonstrated a deep blood flow imaging setup. We show that our system can recover structures as deep as 6 mm, with higher resolution than traditional approaches. With the help of in vivo experiments, we validate that our system is sensitive to actual changes in blood flow induced by arm occlusion. We hope that our work will find its utility in monitoring blood perfusion for peripheral vascular diseases as well as wound-healing applications.

Funding. National Science Foundation (Grant - NSF-1730574).

Acknowledgement. This work was funded by Expeditions (Grant - NSF-1730574).

Disclosures. The authors declare no conflict of interest.

Data availability. Data underlying the results presented in this paper are not publicly available at this time but may be obtained from the authors upon reasonable request.

References

1. M. P. Hartung, T. M. Grist, and C. J. François, "Magnetic resonance angiography: current status and future directions," *J. Cardiovasc. Magn. Reson.* **13**(1), 19 (2011).
2. O. Shwaiki, B. Rashwan, M. A. Fink, L. Kirksey, S. Gadani, K. Karuppasamy, C. Melzig, D. Thompson, G. D'Amico, F. Rengier, and S. Partovi, "Lower extremity CT angiography in peripheral arterial disease: from the established approach to evolving technical developments," *The Int. J. Cardiovasc. Imaging* **37**(10), 3101–3114 (2021).
3. R. C. Mathew and C. M. Kramer, "Recent advances in magnetic resonance imaging for peripheral artery disease," *Vasc. Med.* **23**(2), 143–152 (2018).
4. H. K. Pannu, R. E. Thompson, J. Phelps, C. A. Magee, and E. K. Fishman, "Optimal contrast agents for vascular imaging on computed tomography," *Acad. Radiol.* **12**(5), 576–584 (2005).
5. V. Rajan, B. Varghese, T. G. van Leeuwen, and W. Steenbergen, "Review of methodological developments in laser doppler flowmetry," *Lasers Med. Sci.* **24**(2), 269–283 (2009).
6. T. Ishii, S. Takabe, Y. Yanagawa, Y. Ohshima, Y. Kagawa, A. Shibata, and K. Oyama, "Laser doppler blood flowmeter as a useful instrument for the early detection of lower extremity peripheral arterial disease in hemodialysis patients: an observational study," *BMC Nephrol.* **20**(1), 470 (2019).
7. A. K. Murray, "Laser doppler imaging: a developing technique for application in the rheumatic diseases," *Rheumatology* **43**(10), 1210–1218 (2004).
8. D. A. Boas, L. E. Campbell, and A. G. Yodh, "Scattering and imaging with diffusing temporal field correlations," *Phys. Rev. Lett.* **75**(9), 1855–1858 (1995).
9. D. A. Boas and A. G. Yodh, "Spatially varying dynamical properties of turbid media probed with diffusing temporal light correlation," *J. Opt. Soc. Am. A* **14**(1), 192 (1997).
10. W. Liu, R. Qian, S. Xu, P. C. Konda, J. Jönsson, M. Harfouche, D. Borycki, C. Cooke, E. Berrocal, Q. Dai, H. Wang, and R. Horstmeyer, "Fast and sensitive diffuse correlation spectroscopy with highly parallelized single photon detection," *APL Photonics* **6**(2), 026106 (2021).
11. M. Kumar, J. W. Suliburk, A. Veeraraghavan, and A. Sabharwal, "PulseCam: a camera-based, motion-robust and highly sensitive blood perfusion imaging modality," *Sci. Rep.* **10**(1), 1 (2020).
12. V. V. Zaytsev, S. V. Miridonov, O. V. Mamontov, and A. A. Kamshilin, "Contactless monitoring of the blood-flow changes in upper limbs," *Biomed. Opt. Express* **9**(11), 5387 (2018).
13. A. A. Kamshilin, V. Teplov, E. Nippolainen, S. Miridonov, and R. Giniatullin, "Variability of microcirculation detected by blood pulsation imaging," *PLoS One* **8**(2), e57117 (2013).
14. T. Dragojević, E. E. V. Rosas, J. L. Hollmann, J. P. Culver, C. Justicia, and T. Durduran, "High-density speckle contrast optical tomography of cerebral blood flow response to functional stimuli in the rodent brain," *Neurophotonics* **6**(04), 1 (2019).
15. M. Zhao, S. Mazdeyasna, C. Huang, N. Agochukwu-Nwubah, A. Bonaroti, L. Wong, and G. Yu, "Noncontact speckle contrast diffuse correlation tomography of blood flow distributions in burn wounds: A preliminary study," *Mil. Medicine* **185**(Supplement_1), 82–87 (2020).
16. H. Cheng, Y. Yan, and T. Q. Duong, "Temporal statistical analysis of laser speckle images and its application to retinal blood-flow imaging," *Opt. Express* **16**(14), 10214 (2008).
17. J. C. Ramirez-San-Juan, C. Regan, B. Coyotl-Ocelotl, and B. Choi, "Spatial versus temporal laser speckle contrast analyses in the presence of static optical scatterers," *J. Biomed. Opt.* **19**(10), 106009 (2014).
18. J. Qiu, "Spatiotemporal laser speckle contrast analysis for blood flow imaging with maximized speckle contrast," *J. Biomed. Opt.* **15**(1), 016003 (2010).
19. M. A. Davis, S. M. S. Kazmi, and A. K. Dunn, "Imaging depth and multiple scattering in laser speckle contrast imaging," *J. Biomed. Opt.* **19**(8), 086001 (2014).

20. D.-Y. Li, Q. Xia, T.-T. Yu, J.-T. Zhu, and D. Zhu, "Transmissive-detected laser speckle contrast imaging for blood flow monitoring in thick tissue: from monte carlo simulation to experimental demonstration," *Light: Sci. Appl.* **10**(1), 241 (2021).
21. C. Regan, C. Hayakawa, and B. Choi, "Momentum transfer monte carlo for the simulation of laser speckle imaging and its application in the skin," *Biomed. Opt. Express* **8**(12), 5708 (2017).
22. E. Du, S. Shen, A. Qiu, and N. Chen, "Line scan spatial speckle contrast imaging and its application in blood flow imaging," *Appl. Sci.* **11**(22), 10969 (2021).
23. H. He, Y. Tang, F. Zhou, J. Wang, Q. Luo, and P. Li, "Lateral laser speckle contrast analysis combined with line beam scanning illumination to improve the sampling depth of blood flow imaging," *Opt. Lett.* **37**(18), 3774 (2012).
24. E. Du, S. Shen, S. P. Chong, and N. Chen, "Multifunctional laser speckle imaging," *Biomed. Opt. Express* **11**(4), 2007 (2020).
25. H. M. Varma, C. P. Valdes, A. K. Kristoffersen, J. P. Culver, and T. Durduran, "Speckle contrast optical tomography: A new method for deep tissue three-dimensional tomography of blood flow," *Biomed. Opt. Express* **5**(4), 1275 (2014).
26. C. Huang, S. Mazdeyasna, L. Chen, E. G. A. Jawdeh, H. S. Bada, K. E. Saatman, L. Chen, and G. Yu, "Noninvasive noncontact speckle contrast diffuse correlation tomography of cerebral blood flow in rats," *NeuroImage* **198**, 160–169 (2019).
27. U. Tricoli, C. M. Macdonald, T. Durduran, A. Da Silva, and V. A. Markel, "Diffuse correlation tomography in the transport regime: A theoretical study of the sensitivity to brownian motion," *Phys. Rev. E* **97**(2), 022408 (2018).
28. C. Z. Jafari, S. A. Mihelic, S. Engelmann, and A. K. Dunn, "High-resolution three-dimensional blood flow tomography in the subdiffuse regime using laser speckle contrast imaging," *J. Biomed. Opt.* **27**(08), 1 (2022).
29. D. A. Boas and A. K. Dunn, "Laser speckle contrast imaging in biomedical optics," *J. Biomed. Opt.* **15**(1), 011109 (2010).
30. D. A. Boas, "Diffuse photon probes of structural and dynamical properties of turbid media: Theory and biomedical applications," in *University of Pennsylvania*, (1996).
31. D. A. Boas, S. Sakadzic, J. Selb, P. Farzam, M. A. Franceschini, and S. A. Carp, "Establishing the diffuse correlation spectroscopy signal relationship with blood flow," *Neurophotonics* **3**(3), 031412 (2016).
32. Q. Fang and D. A. Boas, "Monte carlo simulation of photon migration in 3d turbid media accelerated by graphics processing units," *Opt. Express* **17**(22), 20178 (2009).
33. R. Yao, X. Intes, and Q. Fang, "Direct approach to compute jacobians for diffuse optical tomography using perturbation monte carlo-based photon "replay"," *Biomed. Opt. Express* **9**(10), 4588 (2018).
34. A. Sassaroli, "Fast perturbation monte carlo method for photon migration in heterogeneous turbid media," *Opt. Lett.* **36**(11), 2095 (2011).
35. C. Liu, A. K. Maity, A. W. Dubrawski, A. Sabharwal, and S. G. Narasimhan, "High resolution diffuse optical tomography using short range indirect subsurface imaging," in *2020 IEEE International Conference on Computational Photography (ICCP)*, (IEEE, 2020).
36. J.-P. Bouchard, I. Veilleux, R. Jedidi, I. Noiseux, M. Fortin, and O. Mermut, "Reference optical phantoms for diffuse optical spectroscopy part 1 – error analysis of a time resolved transmittance characterization method," *Opt. Express* **18**(11), 11495 (2010).
37. P. G. Vaz, A. Humeau-Heurtier, E. Figueiras, C. Correia, and J. Cardoso, "Effect of static scatterers in laser speckle contrast imaging: an experimental study on correlation and contrast," *Phys. Med. Biol.* **63**(1), 015024 (2017).
38. N. Golubova, E. Potapova, E. Seryogina, and V. Dremin, "Time–frequency analysis of laser speckle contrast for transcranial assessment of cerebral blood flow," *Biomed. Signal Process. Control.* **85**, 104969 (2023).
39. S. Mazdeyasna, C. Huang, M. Zhao, N. B. Agochukwu, A. A. Bahrani, L. Wong, and G. Yu, "Noncontact speckle contrast diffuse correlation tomography of blood flow distributions in tissues with arbitrary geometries," *J. Biomed. Opt.* **23**(09), 1 (2018).
40. C. P. Valdes, H. M. Varma, A. K. Kristoffersen, T. Dragojevic, J. P. Culver, and T. Durduran, "Speckle contrast optical spectroscopy, a non-invasive, diffuse optical method for measuring microvascular blood flow in tissue," *Biomed. Opt. Express* **5**(8), 2769 (2014).
41. E. Zherebtsov, V. Dremin, A. Popov, A. Doronin, D. Kurakina, M. Kirillin, I. Meglinski, and A. Bykov, "Hyperspectral imaging of human skin aided by artificial neural networks," *Biomed. Opt. Express* **10**(7), 3545 (2019).
42. S. J. Kirkpatrick, D. D. Duncan, and E. M. Wells-Gray, "Detrimental effects of speckle-pixel size matching in laser speckle contrast imaging," *Opt. Lett.* **33**(24), 2886 (2008).
43. W. Heeman, W. Steenbergen, G. M. van Dam, and E. C. Boerma, "Clinical applications of laser speckle contrast imaging: a review," *J. Biomed. Opt.* **24**(08), 1 (2019).
44. D. D. Duncan and S. J. Kirkpatrick, "Can laser speckle flowmetry be made a quantitative tool?" *J. Opt. Soc. Am. A* **25**(8), 2088 (2008).
45. D. D. Duncan, S. J. Kirkpatrick, and J. C. Gladish, "What is the proper statistical model for laser speckle flowmetry?" in *SPIE Proceedings*, V. V. Tuchin and L. V. Wang, eds. (SPIE, 2008).
46. J. Tang, S. E. Erdener, B. Li, B. Fu, S. Sakadzic, S. A. Carp, J. Lee, and D. A. Boas, "Shear-induced diffusion of red blood cells measured with dynamic light scattering-optical coherence tomography," *J. Biophotonics* **11**(2), e201700070 (2018).
47. J. Liu, H. Wang, P. Wang, Z. Jin, W. Li, H. Zhang, Z. Shen, and D. Xiong, "Establishing the quantitative relationship between diffuse speckle contrast analysis signals with absolute blood flow," *Biomed. Opt. Express* **9**(10), 4792 (2018).

48. H. Niu, F. Tian, Z.-J. Lin, and H. Liu, "Development of a compensation algorithm for accurate depth localization in diffuse optical tomography," *Opt. Lett.* **35**(3), 429 (2010).
49. F. Tian and H. Liu, "Depth-compensated diffuse optical tomography enhanced by general linear model analysis and an anatomical atlas of human head," *NeuroImage* **85**, 166–180 (2014).
50. A. Mangraviti, F. Volpin, J. Cha, S. I. Cunningham, K. Raje, M. J. Brooke, H. Brem, A. Olivi, J. Huang, B. M. Tyler, and A. Rege, "Intraoperative laser speckle contrast imaging for real-time visualization of cerebral blood flow in cerebrovascular surgery: results from pre-clinical studies," *Sci. Rep.* **10**(1), 7614 (2020).
51. A. B. Parthasarathy, E. L. Weber, L. M. Richards, D. J. Fox, and A. K. Dunn, "Laser speckle contrast imaging of cerebral blood flow in humans during neurosurgery: a pilot clinical study," *J. Biomed. Opt.* **15**(6), 066030 (2010).
52. R. Bi, Y. Du, G. Singh, J.-H. Ho, S. Zhang, A. B. E. Attia, X. Li, and M. C. Olivo, "Fast pulsatile blood flow measurement in deep tissue through a multimode detection fiber," *J. Biomed. Opt.* **25**(05), 1 (2020).
53. C. Regan, B. Y. Yang, K. C. Mayzel, J. C. Ramirez-San-Juan, P. Wilder-Smith, and B. Choi, "Fiber-based laser speckle imaging for the detection of pulsatile flow," *Lasers Surg. Med.* **47**(6), 520–525 (2015).
54. J. Bunke, A. Merdasa, M. Stridh, P. Rosenquist, J. Berggren, J. E. Hernandez-Palacios, U. Dahlstrand, N. Reistad, R. Sheikh, and M. Malmjö, "Hyperspectral and laser speckle contrast imaging for monitoring the effect of epinephrine in local anesthetics in oculoplastic surgery," *Ophthalmic Plast. & Reconstr. Surg.* **38**(5), 462–468 (2022).